







Low pump power coherent supercontinuum generation in heavy metal oxide solid-core photonic crystal fibers infiltrated with carbon tetrachloride covering 930–2500 nm

HIEU VAN LE,¹  VAN THUY HOANG,^{2,3,*}  GRZEGORZ STĘPNIIEWSKI,^{3,4} TRUNG LE CANH,² NGOC VO THI MINH,² RAFAŁ KASZTELANIC,^{3,4}  MARIUSZ KLIMCZAK,³  JACEK PNIEWSKI,³  KHOA XUAN DINH,² ALEXANDER M. HEIDT,⁵ AND RYSZARD BUCZYŃSKI^{3,4} 

¹Faculty of Natural Sciences, Hong Duc University, 565 Quang Trung Street, Thanh Hoa City, Vietnam

²Department of Physics, Vinh University, 182 Le Duan, Vinh City, Vietnam

³Faculty of Physics, University of Warsaw, Pasteura 5, 02-093 Warsaw, Poland

⁴Lukasiewicz Research Network - Institute of Microelectronic and Photonics, Aleja Lotników 32/46, 02-668 Warsaw, Poland

⁵Institute of Applied Physics, University of Bern, Sidlerstrasse 5, 3012 Bern, Switzerland

*thuyhv@vinhuni.edu.vn

Abstract: All-normal dispersion supercontinuum (ANDi SC) generation in a lead-bismuth-gallate glass solid-core photonic crystal fiber (PCF) with cladding air-holes infiltrated with carbon tetrachloride (CCl_4) is experimentally investigated and numerically verified. The liquid infiltration results in additional degrees of freedom that are complimentary to conventional dispersion engineering techniques and that allow the design of soft-glass ANDi fibers with an exceptionally flat near-zero dispersion profile. The unique combination of high nonlinearity and low normal dispersion enables the generation of a coherent, low-noise SC covering 0.93–2.5 μm requiring only 12.5 kW of pump peak power delivered by a standard ultrafast erbium-fiber laser with 100 MHz pulse repetition rate (PRR). This is a much lower peak power level than has been previously required for the generation of ANDi SC with bandwidths exceeding one octave in silica- or soft-glass fibers. Our results show that liquid-composite fibers are a promising pathway for scaling the PRR of ANDi SC sources by making the concept accessible to pump lasers with hundreds of megahertz of gigahertz PRR that have limited peak power per pulse but are often required in applications such as high-speed nonlinear imaging, optical communications, or frequency metrology. Furthermore, due to the overlap of the SC with the major gain bands of many rare-earth fiber amplifiers, our source could serve as a coherent seed for low-noise ultrafast lasers operating in the short-wave infrared spectral region.

© 2021 Optica Publishing Group under the terms of the [Optica Open Access Publishing Agreement](#)

1. Introduction

Supercontinuum generation (SCG) in optical fibers with high brightness, coherence, and large spectral bandwidth has been used for a wide set of applications, such as optical coherence tomography [1,2], frequency metrology [3,4] and frequency comb generation [5]. In particular, SCG with high temporal coherence can be used in nonlinear pulse compression [6,7], time-resolved spectroscopy in multibeam pump-probe techniques [8], two-dimensional white-light spectroscopy [9] or multimodal biophotonic imaging [10,11]. In this context, optical fibers with an all-normal dispersion (ANDi) profile are particularly attractive as they strongly suppress the gain of noise-amplifying incoherent nonlinear effects, such as stimulated Raman scattering or

modulational instability, resulting in lower noise and higher temporal coherence than could be achieved with their conventional, soliton-driven counterparts under most pumping conditions [12]. In addition, ANDi SC typically exhibits flat spectral profiles with high spectral power densities, and preserve a uniform pulse shape with relatively simple spectral phase in the time domain, which is easily compressible to the few-cycle regime [6,7]. Thus, the further development of ANDi SC sources is expected to benefit especially those applications in which spectral uniformity, the temporal profile or the stability of the SC is of importance and that have hence struggled to incorporate the noise-sensitive and complex conventional SC sources [13].

However, ANDi SC sources usually require more powerful pump lasers than conventional, soliton-driven SC sources for the generation of equal spectral bandwidths [12]. Typically, peak powers in the order of 100 kW are necessary to obtain octave-spanning SC spectra when using silica as the nonlinear fiber material [14–16]. Consequently, the substantial benefits of ANDi SCG have been out of reach for the nonlinear spectral broadening of ultrafast lasers with hundreds of megahertz or gigahertz repetition rate, which are often required in applications such as high-speed nonlinear imaging, optical communications, or frequency metrology, but have limited peak power per pulse.

An attractive route of reducing the peak power required for ANDi SCG is the use of nonlinear fibers made of soft glasses with large nonlinear refractive indices, such as silicate, tellurite and chalcogenide glasses [17]. However, these materials typically exhibit relatively long zero-dispersion wavelengths and steep normal dispersion in the near-IR, which severely limit the flatness of the dispersion profile achievable with conventional dispersion engineering methods, and consequently also the obtainable ANDi SC spectral bandwidth.

Here, we show that a simple post-processing step in the form of infiltrating the cladding air-holes of solid-core soft-glass photonic crystal fibers (PCF) with liquids results in additional degrees of freedom that overcome these limitations and that can be exploited to design soft-glass ANDi fibers with exceptionally flat and near-zero dispersion profile. The unique combination of high nonlinearity and low dispersion gives rise to strong nonlinear spectral broadening dynamics and allows the reduction of the peak power to the 10 kW level while maintaining spectral bandwidths exceeding one octave.

We report ANDi SCG in a lead-bismuth-gallate (PBG) glass PCF infiltrated with carbon tetrachloride (CCl_4). While the air-filled fiber has a ZDW in the near-IR, we show that simple infiltration of the cladding air-holes with CCl_4 shifts its chromatic dispersion into the low and flat all-normal dispersion range. Our approach combines a host material with nonlinear refractive index $10\times$ higher than silica [18,19] with the high transparency of CCl_4 from the visible to mid-IR [20], and thus overcomes the limitations observed in earlier studies using silica PCF infiltrated by water [16]. We numerically and experimentally study SCG in the air-filled and infiltrated fibers, and show that the infiltrated fiber generates a high-quality, coherent ANDi SC with a -10 dB spectral bandwidth covering 0.9–2.5 μm requiring only 12.5 kW pump peak power delivered by a standard commercial Er: fiber femtosecond laser system operating with 100 MHz repetition rate.

2. Fiber layout design and dispersion engineering

2.1. Fiber development

We consider a solid core PCF with regular hexagonal lattice of air-holes in the cladding region, which are all infiltrated with CCl_4 . As shown in Fig. 1, the cladding consists of 9 rings of holes, where the fiber dispersion is predominantly determined by the diameter of the holes in the first ring (d_1). The diameter d_2 of holes in the second ring is larger than others in order to reduce the confinement losses. Thus, the preliminary simulation to optimize the dispersion characteristics considers only the variation of d_1 and lattice constant Λ_1 of the first ring, while the size of holes in the outer rings is kept constant. The value of d_2 , d_3 , and Λ_3 are 1.7 μm , 1.4 μm , and 1.75 μm ,

respectively. A similar, unfilled fiber design has been studied in context of soliton fission-based SCG in previous work [18], and is generally based on the concept proposed by Saitoh *et al.* [21].

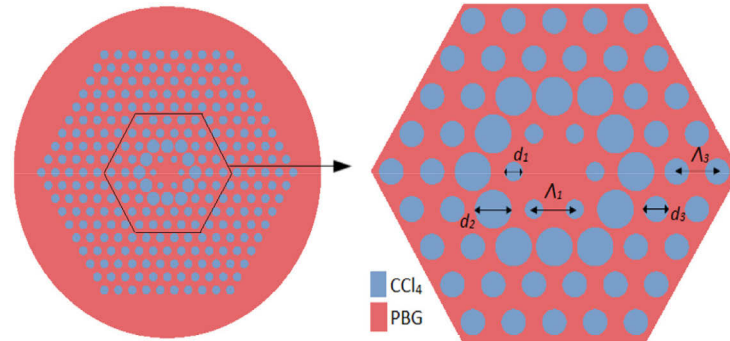


Fig. 1. The schematic of the structure of the analyzed PCF. All of the holes in the cladding region are infiltrated with CCl_4 .

The substrate of the fiber is an in-house developed lead-bismuth-gallate glass. Figure 2 displays its refractive index and transmission as well as the refractive index of CCl_4 [18,19,22].

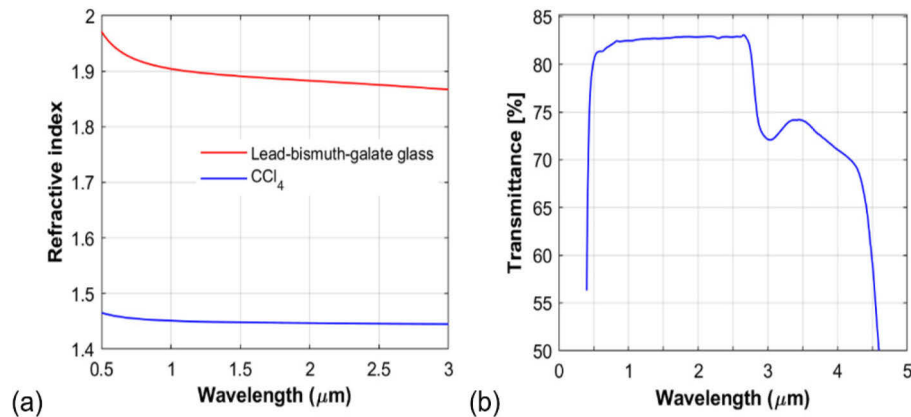


Fig. 2. (a) The refractive index of PBG glass and CCl_4 , taken after [18,22]. (b) Transmittance of a 2 mm thick PBG glass sample.

The dispersion of the PCF with various values of Λ_1 and d_1 is numerically simulated using the Finite Difference Eigenmode method (FDM). Λ_1 and d_1 are varied in the range of 1.2–1.7 μm and 0.6–0.9 μm , respectively. The possibility of controlling the lattice constant and the diameter of the holes in the cladding region allow the precise shaping of the dispersion characteristics in the investigated wavelength range. As shown in Fig. 3, almost all of the unfilled fibers have anomalous dispersion from near-IR towards longer wavelengths. The unfilled fiber with $\Lambda_1 = 1.2 \mu\text{m}$ and $d_1 = 0.75 \mu\text{m}$ has all-normal dispersion, but the dispersion shape is not flat, which limits the possible spectral broadening during SCG. On the contrary, the CCl_4 -filled PCF have all-normal and flat dispersion in the near- and mid-IR range, according to our calculations. In particular, the CCl_4 -filled PCF with $\Lambda_1 = 1.5 \mu\text{m}$ and $d_1 = 0.75 \mu\text{m}$ has a flat near-zero all-normal dispersion profile in the investigated wavelength range. Therefore, the fiber with those parameters is selected for further analysis as it has the potential for broadband ANDi SCG.

After the preliminary fiber design, the optimized PCF structure was fabricated using the conventional stack-and-draw method [23]. The fabrication procedure involved two main stages.

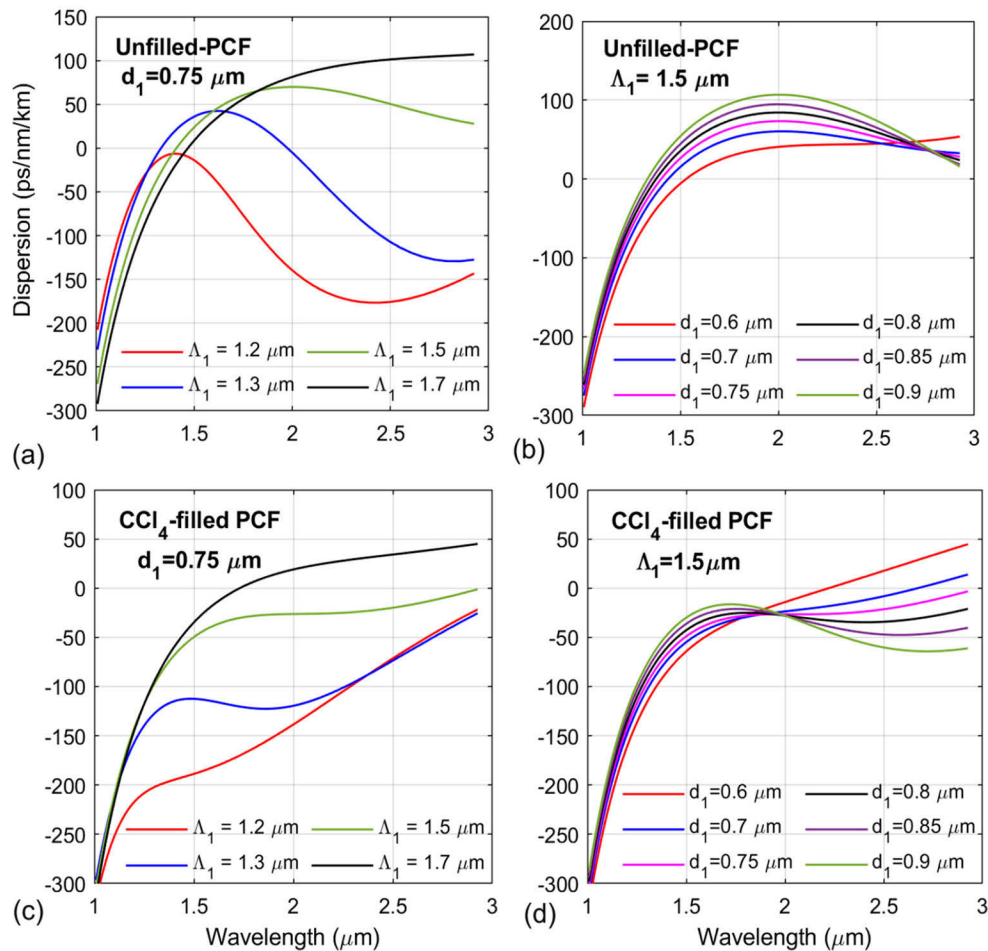


Fig. 3. Simulated dispersion profiles of unfilled PCF with varying Λ_1 (a) and varying hole diameter d_1 (b). Simulated dispersion profiles of CCl_4 -filled PCF with varying Λ_1 (c) and varying hole diameter d_1 (d).

First, the capillaries and rods were stacked to make a preform, which was then drawn to a sub-preform using low pressure to reduce the gaps between the capillaries and rods. Second, the final fiber structure was drawn from the sub-preform, where a selective choice of pressure and temperature scaled down the size of capillaries to those of the designed fiber structure. SEM images of the final PCF are shown in Fig. 4 and the geometrical parameters are listed in Table 1. The core diameter (d_{core}) is measured to approx. $2.12 \mu\text{m}$. The deformations of the air-holes visible in the second cladding ring of the fiber stem from gradients of pressure and temperature in the air-holes during fiber drawing. They result in a moderate shift of the dispersion characteristic with respect to the designed profile. Using numerical simulations we estimated the impact of those deformations and found them to shift the dispersion profile by a maximum of $\pm 15 \text{ ps/nm/km}$ around $D = -15 \text{ ps/nm/km}$ at the wavelength of $\lambda = 2000 \text{ nm}$, assuming that the second-ring air-hole diameter changes within $\pm 0.2 \mu\text{m}$ around $d_2 = 1.6 \mu\text{m}$. Notably, these deformations do not affect the dispersion flatness and the entire characteristic remains normal across all wavelengths of interest.

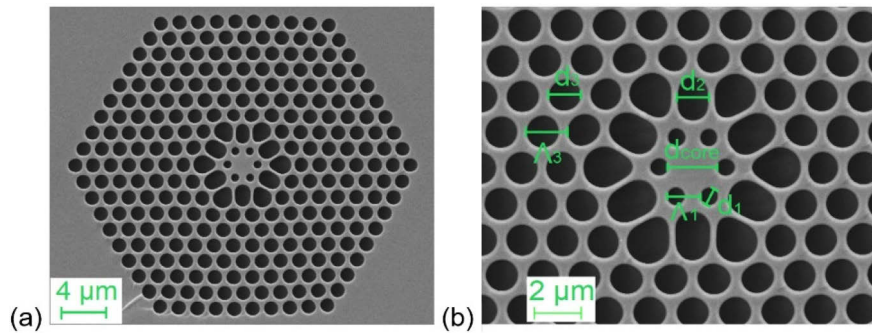


Fig. 4. SEM image of the fabricated PBG-glass PCF subsequently used for CCl_4 infiltration and SCG experiments.

Table 1. The geometrical parameters for the final fiber selected for CCl_4 infiltration and SCG experiments.

Parameter	Value
Lattice constant of the first ring Λ_1 [μm]	1.48
Hole diameter d_1 [μm]	0.74
Hole diameter d_2 [μm]	1.8
Hole diameter d_3 [μm]	1.4
Lattice constant of the outer rings Λ_3 [μm]	1.8
Core diameter (d_{core})	2.12

2.2. Chromatic dispersion and attenuation measurements

The dispersion characteristics of the fabricated air-filled and CCl_4 -filled PCF are measured using a Mach-Zehnder interferometer setup, as detailed in [24]. Details regarding the filling of the fiber and the liquid pump system used during the experiments with the CCl_4 -filled fiber are given in Section 3.2. Figure 5 compares the simulated and measured dispersion characteristics of air-filled and CCl_4 -filled PCF. The experimental results match very well with the simulation. The air-filled PCF has a ZDW at $1.4 \mu\text{m}$, i.e., it exhibits anomalous dispersion in the near-IR and mid-IR range. The dispersion varies from -280 ps/nm/km to 87 ps/nm/km in a wavelength range of $1.0\text{--}2.1 \mu\text{m}$. The liquid infiltration significantly shifts the dispersion to the normal regime over the entire investigated wavelength range and flattens the dispersion profile. The dispersion varies from -280 ps/nm/km to -15 ps/nm/km in a wavelength range of $1.00\text{--}2.5 \mu\text{m}$.

In contrast to earlier ANDi fiber designs compatible with 1560 nm femtosecond pumping, e.g. all-solid soft glass PCFs [25] or air-hole lattice Ge-doped silica core PCFs [26], where fiber engineering effectively shifted the entire dispersion profile across the dispersion axis, the CCl_4 infiltration of this fiber shifts and flattens mainly the long-wave IR part of the dispersion profile, leading to enhanced spectral broadening towards longer wavelengths in the ANDi SCG dynamics [27]. This reveals the additional degree of freedom in chromatic dispersion design obtained when using liquid infiltration of a PCF lattice, which is complementary to techniques involving all-solid glass lattices or double-period lattices demonstrated earlier [16,21]. The introduction of the liquid can be considered an alternative to an all-solid glass PCFs in cases where it is challenging to thermally match two glass types. When used with a double-period air-hole lattice PCF, liquid infiltration extends the dispersion shaping flexibility substantially.

The attenuation of the investigated fibers is measured using the cut-back method and the results displayed in Fig. 6. Since CCl_4 has high transparency from the visible to the near-IR range, the

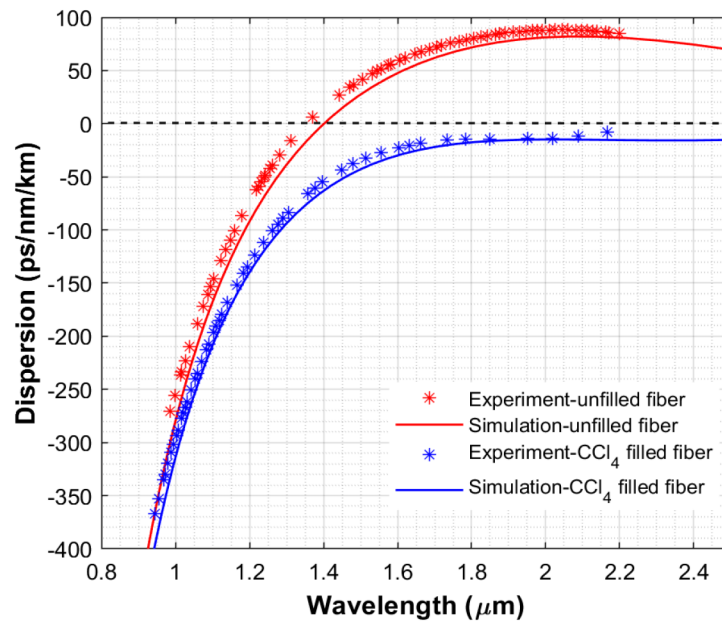


Fig. 5. Simulated and measured chromatic dispersion of the unfilled PCF and CCl_4 -filled PCF.

attenuation of the CCl_4 -filled fiber is similar to that of the unfilled fiber. Both fibers have a high attenuation in the visible range below $0.8 \mu\text{m}$ due to the high absorption of the PBG glass. The attenuation decreases in the near-IR range to 9.7 dB/m and 9.5 dB/m at the pump wavelength of $1.56 \mu\text{m}$ for the CCl_4 -filled and unfilled fibers, respectively. In the long-wavelength range ($\lambda > 2 \mu\text{m}$), the attenuation increases due to confinement losses. While these attenuation figures are relatively high compared to silica PCF, we note that these fibers are intended for SCG using femtosecond pumping, which allows the use of short fiber lengths.

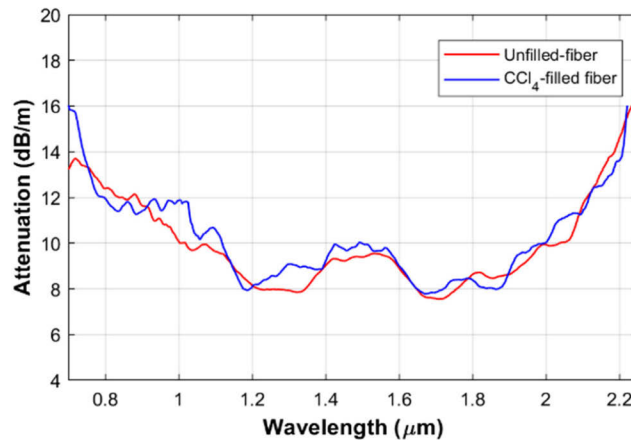


Fig. 6. Measured loss of unfilled and CCl_4 -filled fiber.

3. Supercontinuum generation in developed PCF

3.1. Numerical modelling

Supercontinuum generation in the unfilled and CCl₄-filled PCF are simulated by numerically solving the standard nonlinear Schrödinger equation (GNLSE) in the frequency domain,

$$\partial_z \tilde{A} - i\tilde{\beta}(\omega)\tilde{A} - \frac{\tilde{\alpha}(\omega)}{2}\tilde{A} = i\gamma \left(1 + \frac{\omega - \omega_0}{\omega_0} \right) \tilde{A} \mathcal{F} \left[\int_{-\infty}^{\infty} R(T') |A(T - T')|^2 dT' \right], \quad (1)$$

where $\tilde{A}(\omega, z)$ is the spectral amplitude function of the pulse. The left side of Eq. (1) contains the effects of dispersion ($\tilde{\beta}$) and loss ($\tilde{\alpha}$), where we use the measured values presented in Figs. 6 and 7. The right side of Eq. (1) contains the nonlinear terms, where the nonlinear coefficient $\gamma(\omega) = 2\pi n_2 / (\lambda A_{eff}(\omega))$ depends in the nonlinear refractive index of the PBG glass, $n_2 = 2 \times 10^{-19} \text{ m}^2/\text{W}$ at 1064 nm [18,19], and the effective mode area A_{eff} . Compared to the unfilled fiber, the infiltration of the cladding holes with CCl₄ leads to a reduction of the refractive index contrast between cladding and core. Consequently, the CCl₄-filled fiber has larger effective mode area for the fundamental mode and a lower nonlinear coefficient than the unfilled fiber, as shown in Fig. 7. Nevertheless, due to the high nonlinear refractive index of PBG glass both filled and unfilled fibers have a relatively high nonlinear coefficient γ of $206 \text{ W}^{-1}\text{km}^{-1}$ and $250 \text{ W}^{-1}\text{km}^{-1}$ at the wavelength of 1560 nm, respectively.

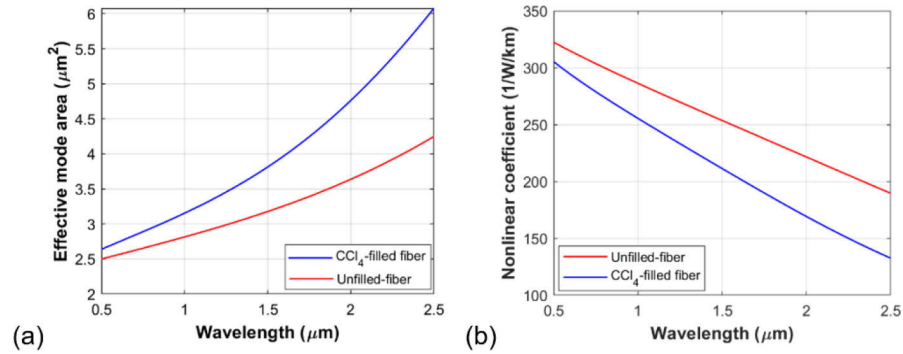


Fig. 7. (a) The effective mode area and (b) nonlinear coefficient of unfilled and CCl₄-filled PCF.

The Raman response function $R(T)$ in Eq. (1) is modelled by a single Lorentzian line and is given by

$$R(T) = (1 - f_R)\delta(T) + f_R \frac{\tau_1^2 + \tau_2^2}{\tau_1 \tau_2^2} \exp\left(\frac{-T}{\tau_2}\right) \sin\left(\frac{T}{\tau_1}\right) \Theta(T), \quad (2)$$

where $f_R = 0.05$, $\tau_1 = 5.5$ fs, and $\tau_2 = 32$ fs have been determined for PBG glass [18]. $\delta(T)$ is the Dirac delta function, and $\Theta(T)$ is the Heaviside step function. In the model we assume that only the glass as core material contributes significantly to the Raman response of the liquid-filled fiber.

We numerically investigate the coherence characteristics of SCG by making use of the usual definitions of first-order degree of coherence $|g_{12}^{(1)}(\omega)|$ and average coherence $|g_{12}^{(1)}|$, as described e.g. in [28,29]. In our model, we take into account the effects of vacuum noise (shot noise) and the pulse-to-pulse relative intensity noise (RIN). The shot noise is introduced by the addition of one photon with a random phase per each simulation bin [29], while RIN is defined as the fluctuation of the amplitude and duration of individual laser pulses compared to their mean value. This noise is determined by the pump laser characteristics. We follow the formalism recently proposed in [30] to calculate the coherences with the presence of shot noise and pulse-to-pulse

noise for a set of 20 simulations with independent noise seeds. We do not consider the effects of polarization noise as this is expected to have only minor influence at the short pulse durations used in our experiments [31].

3.2. Experimental setup

The experimental setup to measure SCG in the investigated fibers is shown in Fig. 8. As a pump laser we use an Er: fiber femtosecond laser system (C-fiber HP, Menlo Systems) with a central wavelength of 1560 nm, pulse duration of 90 fs and repetition rate of 100 MHz. The maximum average power was 350 mW, corresponding to maximum pulse energy of 3.5 nJ. The pump beam first passed through the variable neutral-density filter to control the pulse energy coupled into the fiber. The lens L_1 with a focal length of 3.1 mm (Thorlabs- C330TME-C) is used to couple the light into the tested fiber. A coupling efficiency of 20% and 30% is measured for unfilled and CCl_4 -filled fiber, respectively. The output beam is collimated using lens L_2 with a focal length of 4.51 mm (Thorlabs C230TME-C) and then coupled into commercial multimode fiber (Thorlabs-M122L01). The generated SC is recorded using two IR spectrometers: OSA (Hewlett Packard, HP 71451B, wavelength range of 600-1700nm) and Ocean Optics NIRQuest512-2.5 (wavelength range of 900–2500 nm).

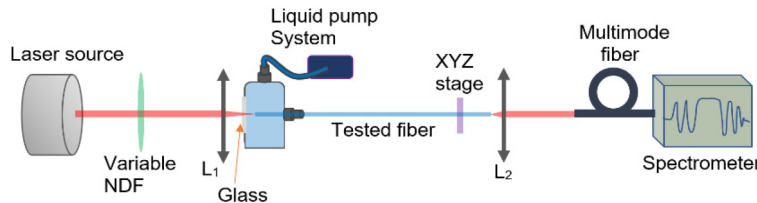


Fig. 8. Schematic of the experimental setup for SCG measurement in the CCl_4 -filled fiber.

In the case of CCl_4 -filled fiber, a microfluidic pump system maintaining a constant pressure of 10 kPa is used to minimize microbubble-related effects and suppress thermal effects in the liquid in high-repetition rate pumping conditions. CCl_4 is infiltrated into all air-holes in the cladding region of the tested fiber by capillary action and the pressure of the liquid pump system. The input end of the fiber was placed in a custom optical-liquid feed-through holder, while the output end was fixed in a standard, bare fiber, free space holder. While this simplification allowing the continuously pumped liquid to drip out of the fiber at the optical output is acceptable in these proof-of-principle experiments, any practical application would require the introduction of a second feed through at the fiber output in combination with a closed-loop system.

We note that manipulation of optical properties of air-hole lattice fibers using infiltration with liquids can be challenging due to possible formation of air-bubbles. The complex structure of the fiber lattice and the small hole diameter below the diffraction limit make it difficult to monitor the filling of individual holes, e.g. using direct imaging or the scattered light method reported previously [32]. Based on experiments reported in [33], we estimate that it takes approximately 15 minutes to fully fill the fiber sample, and all experiments were conducted following a corresponding delay after starting the liquid pump. Furthermore, a continuous flow was maintained to average out the impact of any microbubble formation during experiments.

The investigated fibers are not single mode at pump wavelength 1560 nm. Based on our numerical analysis, the unfilled fiber guides three modes (LP_{01} , LP_{11} , and LP_{21}), while the CCl_4 -filled fiber guides only two modes (LP_{01} and LP_{11}). However, the effective refractive index of the fundamental mode (LP_{01}) is significantly different from that of the higher-order mode (LP_{11}) at $\lambda = 1560$ nm ($\Delta n_{\text{eff}} = 0.055$ for the CCl_4 -filled fiber), which prevents energy transfer between the modes if the fundamental mode is selectively excited, which is achieved by

modifying the position of lens L_1 . The single mode guidance in the CCl_4 -filled fiber is tested at low pulse energies by imaging the far-field output on a CCD camera and comparing the intensity distribution at the center of a beam with a Gaussian function, as shown in Fig. 9. The good match between experimental data and the Gaussian function confirms the predominantly single-mode guidance of the fiber.

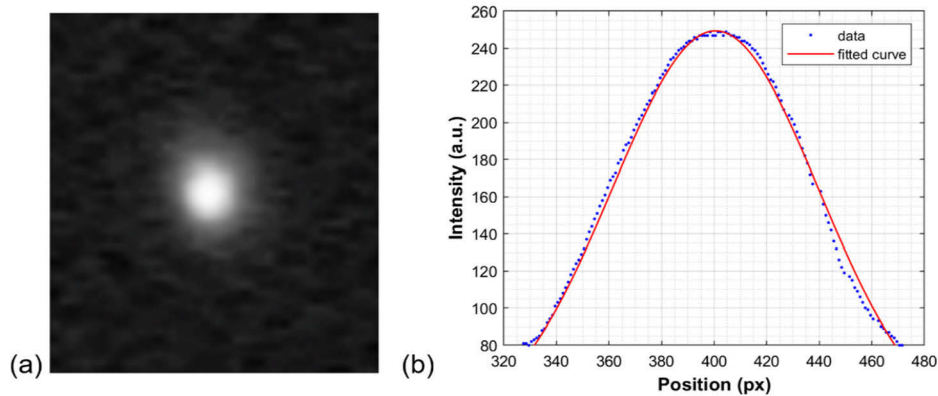


Fig. 9. (a) Far-field image of the output beam from the CCl_4 -filled fiber. (b) Intensity distribution at the beam center fitted with a Gaussian profile).

3.3. Discussion

3.3.1. Air-filled PCF

The bare PCF has a ZDW at $1.4\ \mu\text{m}$ and anomalous dispersion at the pump wavelength. Therefore, SCG in this fiber is determined by well-known soliton dynamics, which are summarized in the numerical simulations in Fig. 10 for an input pulse energy of $0.12\ \text{nJ}$ (peak power $P_0 = 1.3\ \text{kW}$) and a fiber length of $16\ \text{cm}$, matching the experimental conditions. The SCG dynamics are dominated by soliton fission occurring after approx. $2\ \text{cm}$. Consequently, the SC spectrum is formed by the signatures of red-shifting Raman solitons on the long-wavelength edge and phase-matched dispersive waves (DW) on the short-wavelength edge [34,35]. The spectrogram after $16\ \text{cm}$ of propagation follows the concave shape of the group velocity profile of the fiber, showing clearly the individual soliton signatures as well as the long DW tail on the trailing edge.

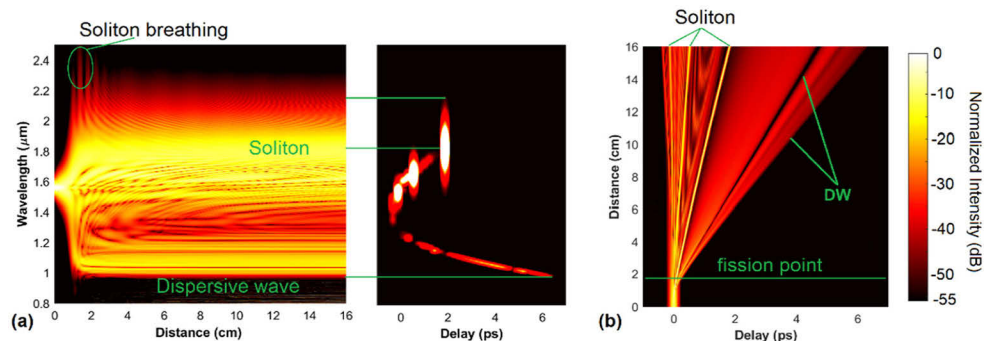


Fig. 10. (a) Spectral evolution of SCG in unfilled fiber and spectrogram of the SC pulse after $16\ \text{cm}$ of propagation. (b) Temporal evolution of the pulse during propagation. An input pulse energy of $0.12\ \text{nJ}$ ($1.3\ \text{kW}$ peak power) and pulse duration of $90\ \text{fs}$ are considered.

Figure 11(a, b) compare the measured and simulated SC spectra with input pulse energies of 0.12 nJ and 0.7 nJ (1.3 kW and 7.8 kW peak power), respectively. In the low power case, the -20 dB spectral bandwidth covers the range 0.96 μm - 1.97 μm , broadening to 0.8 μm - 2.5 μm with higher pump power. In both cases, the simulated SC bandwidth matches very well with the experimental data. The differences in the spectral structure are attributed to the pump pulse shape: while the simulations use pump pulses with ideal (gaussian) shape, the pulses emitted by the Er:fiber laser contain side-pulses and pedestals, which can have a significant influence on the spectral and temporal fine structure of the generated SC [36].

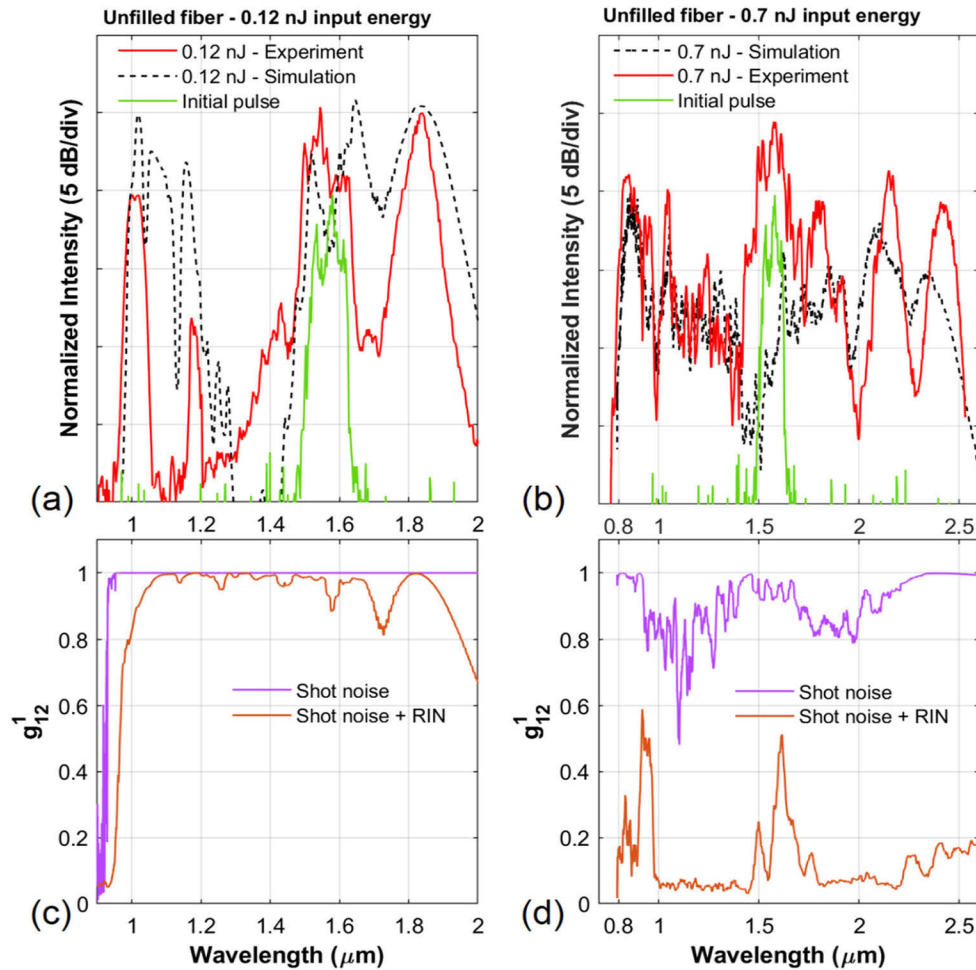


Fig. 11. The simulated and experimental results of SCG in the unfilled fiber with (a) 0.12 nJ and (b) 0.7 nJ input pulse energy. Numerically simulated coherence considering only shot noise or shot noise and additional input pulse RIN with (c) 0.12 nJ and (d) 0.7 nJ input pulse energy. 16 cm fiber length, pump wavelength at 1560 nm, and pulse duration of 90 fs are considered.

Figure 11(c, d) present the simulated coherence properties of the SC with the effects of shot noise and RIN, where RIN is derived from the intensity fluctuations of input pulses with root-mean-square (rms) of 0.5%. While in the low-energy case the coherence remains high with $\langle g_{12}^1 \rangle = 0.95$, the coherence collapses for high-energy pumping, especially when the pump pulse RIN is included ($\langle g_{12}^1 \rangle = 0.11$). This behavior can be understood by considering the characteristic

length scales of the pulse broadening dynamics,

$$L_D = \frac{t_0^2}{|\beta_2|} L_{NL} = \frac{1}{\gamma P_0}, N = \sqrt{\frac{L_D}{L_{NL}}}, L_{fiss} = \frac{L_D}{N}, L_{MI} \approx 16L_{NL}, \quad (3)$$

where L_D , L_{NL} , L_{fiss} , L_{MI} are dispersion, nonlinear, soliton fission, and modulation instability characteristics length, respectively. N is the soliton number. P_0 and t_0 are peak power and pulse duration of the input pulse. Table 2 shows the corresponding length scales for both low- and high energy pumping. For the low-energy case, $L_{fiss} < L_{MI}$ implies a dominance of the coherent soliton fission over noise-amplifying incoherent MI dynamics. For the high energy case, MI plays a more dominant role, which leads to the amplification of quantum noise and pump laser noise which is uncorrelated from shot-to-shot, leading to the observed coherence collapse.

3.3.2. CCl₄-filled fiber

The CCl₄-filled fiber has an all-normal dispersion profile in the investigated wavelength range, thus nonlinear spectral broadening dynamics dominated by self-phase modulation (SPM) and optical wave-breaking (OWB) are expected. This is confirmed by the numerical simulations in Fig. 12, which consider an input pulse energy of 1.1 nJ (12.5 kW peak power) and 10 cm fiber length, matching the experimental conditions. While the initial propagation is characterized by the multi-peak spectral structure of SPM, the SC is smoothed by the onset of OWB after 0.75 cm and 4 cm on the short- and long-wavelength edges, respectively. This asymmetry is caused by the dispersion profile of the fiber (Fig. 5), which is extremely flat on the long-wavelength side, delaying the onset of OWB and enhancing the spectral broadening towards the mid-IR. The spectrogram at the end of the fiber is typical for ANDi SC, with every spectral component occupying a unique temporal position within the pulse. The strong chromatic dispersion of the fiber at short wavelengths contributes to a pronounced temporal broadening of the trailing pulse edge.

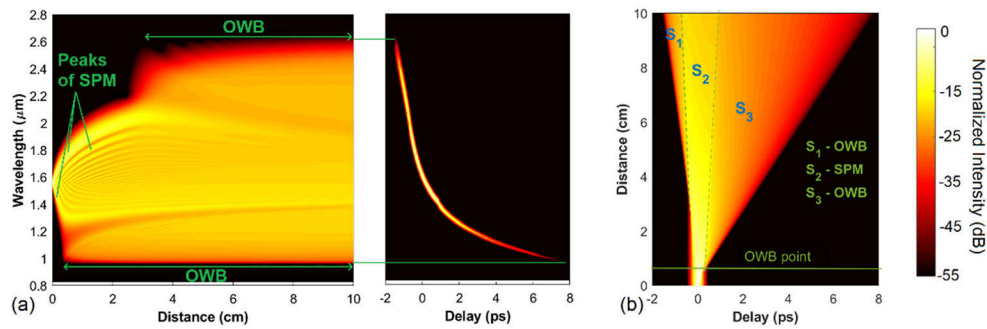


Fig. 12. (a) Spectral evolution of SCG in the CCl₄-filled fiber and spectrogram of the SC pulse after 10 cm of propagation. (b) Temporal evolution of the pulse during propagation. An input pulse energy of 1.1 nJ (12.5 kW peak power) and pulse duration of 90 fs are considered.

Table 2. Characteristic length scales of the unfilled fiber with input pulse energy of 0.12 nJ and 0.7 nJ.

Pulse energy (nJ)	Peak power (kW)	β_2 (ps ² /m)	L_D (cm)	L_{NL} (cm)	N	L_{fiss} (cm)	L_{MI} (cm)
0.12	1.3	0.05	16.5	0.28	8	2	4.6
0.7	7.8	0.05	16.5	0.046	19	0.86	0.74

Figure 13(a, b) compare the simulated and measured ANDi SC with input pulse energies of 0.4 nJ and 1.1 nJ (peak power of 4.5 kW and 12.5 kW), respectively. Similar to the case of the

bare PCF, the bandwidth of measured and simulated spectra match very well, while we attribute differences in the spectral fine structure to the non-ideal pulse shape emitted by the Er: fiber laser [36]. At the -10 dB level, the SC spans the range 1.13 - 2.14 μm for the low power pump, increasing to 0.93 - 2.5 μm for the 12.5 kW peak power pulses.

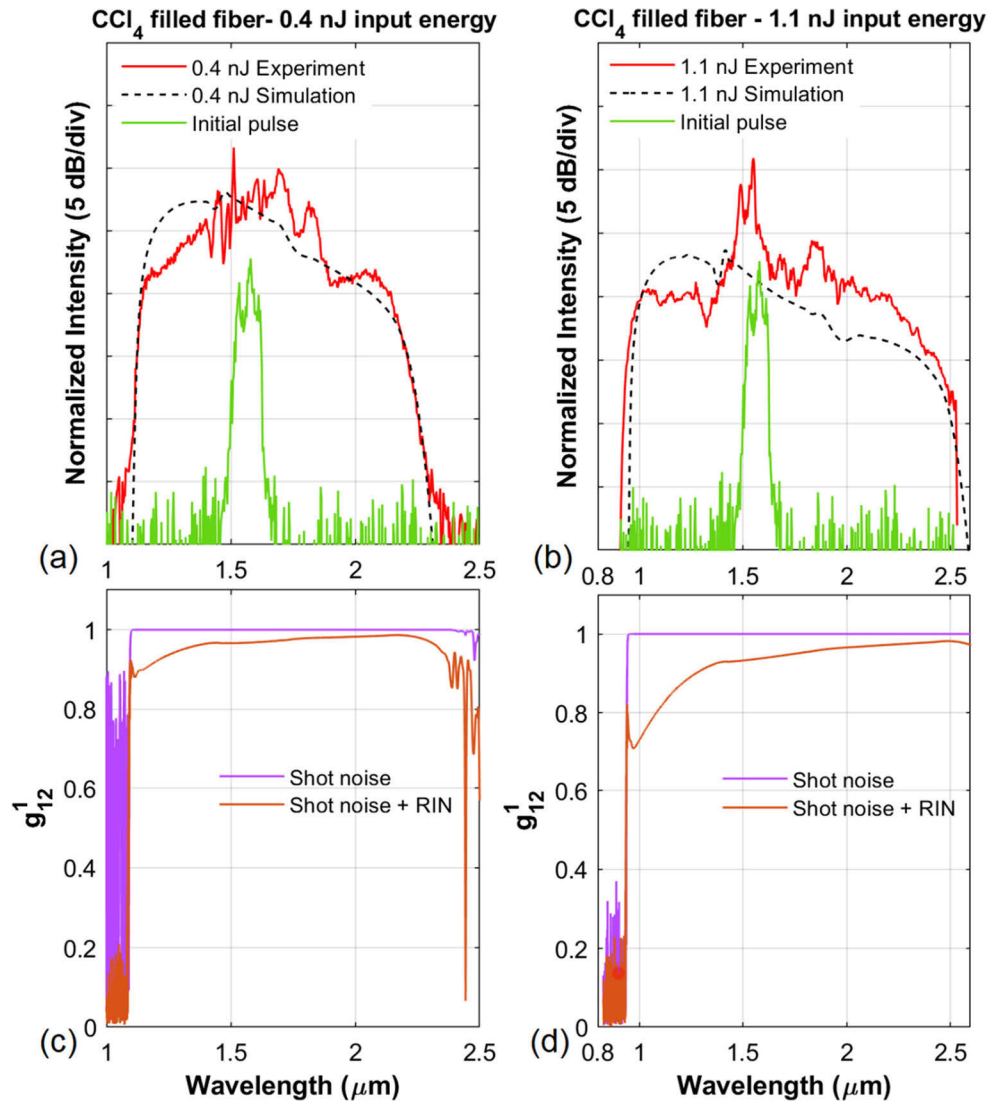


Fig. 13. Simulated and experimental results of SCG in the CCl₄-filled fiber with (a) 0.4 nJ and (b) 1.1 nJ input pulse energy. Numerically simulated coherence considering only shot noise or shot noise and additional input pulse RIN with (c) 0.4 nJ and (d) 1.1 nJ input pulse energy. 10 cm fiber length, pump wavelength at 1560 nm, and pulse duration of 90 fs are considered.

The attenuation of the CCl₄ fiber over a 10 cm long sample does not significantly influence the average power level of the supercontinuum signal. Instead, the main limiting factor is the relatively low coupling efficiency. The supercontinuum signal average power measured at the output of a CCl₄-infiltrated, 10 cm-long PCF was 50 mW.

MI is suppressed in the ANDi regime, resulting in a significant improvement of the coherence as compared to the bare PCF, as shown in Fig. 13(c, d) [34]. Although inclusion of pump laser RIN causes a moderate decrease of the calculated coherence, it has been shown that this effect is caused by a timing-jitter on a time-scale of < 100 attoseconds with no practical relevance for most applications [37].

4. Conclusion

The generation of low-noise, Er: fiber-pumped ANDi SC with such a broad spectral coverage at this low peak power level is quite remarkable and has not been achieved with comparable silica or soft-glass “standard” fibers, i.e. not infiltrated with liquids [16,26,38–40]. From an applications perspective, this development has far-reaching consequences. Firstly, it makes octave-spanning ANDi SCG accessible to applications requiring high repetition rates, such as frequency metrology or high-speed optical coherence tomography. While recent experiments convincingly demonstrated the advantages of ANDi SC over conventional SC in these applications, the scaling of the repetition rate to the typically required values has remained a long-standing challenge to which liquid-cladding soft-glass PCF offer a promising solution, as we show with this work. Secondly, ANDi SCG has recently been considered as a promising approach for extending and power-scaling the excellent low-noise performance and robustness of ultrafast Er: fiber technology to other wavebands. The ANDi SC described in this work spectrally broadens our mode-locked Er: fiber laser to cover all gain bands of rare-earth dopants used in mature optical fiber technology, and thus can serve as a non-solitonic (i.e. virtually noise-free), coherent seed signal for multiple, temporally synchronized ultrafast amplifiers in the 1–2 μm wavelength region with noise levels virtually identical to the Er: fiber seed laser, similar to Thulium- and Thulium-/Holmium-doped amplifiers reported recently [41,42].

Funding. Schweizerischer Nationalfonds zur Förderung der Wissenschaftlichen Forschung (PCEFP2_181222); Narodowe Centrum Nauki (PRELUDIUM-18 UMO-2019/35/N/ST7/01768); National Foundation for Science and Technology Development (103.03-2020.19).

Disclosures. The authors declare no conflicts of interest.

Data availability. Data underlying the results presented in this paper are not publicly available at this time but may be obtained from the authors upon reasonable request.

References

1. G. Humbert, W. J. Wadsworth, S. G. Leon-Saval, J. C. Knight, T. A. Birks, P. St. J. Russell, M. J. Lederer, D. Kopf, K. Wiesauer, E. I. Breuer, and D. Stifter, “Supercontinuum generation system for optical coherence tomography based on tapered photonic crystal fibre,” *Opt. Express* **14**(4), 1596–1603 (2006).
2. N. M. Israelsen, C. R. Petersen, A. Barh, D. Jain, M. Jensen, G. Hanneschläger, P. Tidemand-Lichtenberg, C. Pedersen, A. Podoleanu, and O. Bang, “Real-time high-resolution mid-infrared optical coherence tomography,” *Light Sci Appl* **8**(1), 11 (2019).
3. J. T. Woodward, A. W. Smith, C. A. Jenkins, C. Lin, S. W. Brown, and K. R. Lykke, “Supercontinuum sources for metrology,” *Metrologia* **46**(4), S277–S282 (2009).
4. D. R. Carlson, D. D. Hickstein, A. Lind, J. B. Olson, R. W. Fox, R. C. Brown, A. D. Ludlow, Q. Li, D. Westly, H. Leopardi, T. M. Fortier, K. Srinivasan, S. A. Diddams, and S. B. Papp, “Photonic-Chip Supercontinuum with Tailored Spectra for Counting Optical Frequencies,” *Phys. Rev. Appl.* **8**(1), 014027 (2017).
5. T. Fortier and E. Baumann, “20 years of developments in optical frequency comb technology and applications,” *Commun. Phys.* **2**(1), 153 (2019).
6. S. Demmler, J. Rothhardt, A. M. Heidt, A. Hartung, E. G. Rohwer, H. Bartelt, J. Limpert, and A. Tünnermann, “Generation of high quality, 1.3 cycle pulses by active phase control of an octave spanning supercontinuum,” *Opt. Express* **19**(21), 20151–20158 (2011).
7. Y. Liu, H. Tu, and S. A. Boppart, “Wave-breaking-extended fiber supercontinuum generation for high compression ratio transform-limited pulse compression,” *Opt. Lett.* **37**(12), 2172–2174 (2012).
8. I. Tamer, M. Hellwing, Y. Azamoum, M. Hornung, S. Keppler, F. Schorcht, J. Hein, and M. C. Kaluza, “Few-cycle fs-pumped NOPA with passive ultrabroadband spectral shaping,” *Opt. Express* **28**(13), 19034–19043 (2020).
9. N. M. Kearns, A. C. Jones, M. B. Kunz, R. T. Allen, J. T. Flach, and M. T. Zanni, “Two-dimensional white-light spectroscopy using supercontinuum from an all-normal dispersion photonic crystal fiber pumped by a 70 MHz Yb fiber oscillator,” *J. Phys. Chem. A* **123**(13), 3046–3055 (2019).

10. R. Viljoen, P. Neethling, D. Spangenberg, A. Heidt, H.-M. Frey, T. Feurer, and E. Rohwer, "Implementation of temporal ptychography algorithm, i2PIE, for improved single-beam coherent anti-Stokes Raman scattering measurements," *J. Opt. Soc. Am. B* **37**(11), A259–A265 (2020).
11. K. P. Herdzyk, K. N. Bourdakos, P. B. Johnson, A. P. Lister, A. P. Pitera, C-Y Guo, P. Horak, D. J. Richardson, J. H. Price, and S. Mahajan, "Multimodal spectral focusing CARS and SFG microscopy with a tailored coherent continuum from a microstructured fiber," *Appl. Phys. B* **126**(5), 84 (2020).
12. A. M. Heidt, A. Hartung, and H. Bartelt, "Generation of ultrashort and coherent supercontinuum light pulses in all-normal dispersion fibers," in *The Supercontinuum Laser Source: The Ultimate White Light* (Springer 2016), pp. 247–280.
13. A. Rampur, D. Spangenberg, B. Sierro, P. Hänzi, M. Klimczak, and A. M. Heidt, "Perspective on the next generation of ultra-low noise fiber supercontinuum sources and their emerging applications in spectroscopy, imaging, and ultrafast photonics," *Appl. Phys. Lett.* **118**(24), 240504 (2021).
14. A. M. Heidt, A. Hartung, G. W. Bosman, P. Krok, E. G. Rohwer, H. Schwoerer, and H. Bartelt, "Coherent octave spanning near-infrared and visible supercontinuum generation in all-normal dispersion photonic crystal fibers," *Opt. Express* **19**(4), 3775–3787 (2011).
15. A. Hartung, A. M. Heidt, and H. Bartelt, "Pulse-preserving broadband visible supercontinuum generation in all-normal dispersion tapered suspended-core optical fibers," *Opt. Express* **19**(13), 12275–12283 (2011).
16. T. L. Canh, V. T. Hoang, H. L. Van, D. Pysz, V. C. Long, T. B. Dinh, D. T. Nguyen, Q. H. Dinh, M. Klimczak, R. Kasztelanic, J. Pniewski, R. Buczynski, and K. X. Dinh, "Supercontinuum generation in all-normal dispersion suspended core fiber infiltrated with water," *Opt. Mater. Express* **10**(7), 1733–1748 (2020).
17. T. Sylvestre, E. Genier, A.N. Ghosh, P. Bowen, G. Genty, J. Troles, A. Mussot, A.C. Peacock, M. Klimczak, A.M. Heidt, J.C. Travers, O. Bang, and J.M. Dudley, "Recent advances in supercontinuum generation in specialty optical fibers," *J. Opt. Soc. Am. B* **38**(12), F90–F103 (2021).
18. G. Stępniewski, J. Pniewski, D. Pysz, J. Cimek, R. Stępień, M. Klimczak, and R. Buczyński, "Development of Dispersion-Optimized Photonic Crystal Fibers Based on Heavy Metal Oxide Glasses for Broadband Infrared Supercontinuum Generation with Fiber Lasers," *Sensors* **18**(12), 4127 (2018).
19. J. Cimek, N. Liaros, S. Couris, R. Stępień, M. Klimczak, and R. Buczyński, "Experimental investigation of the nonlinear refractive index of various soft glasses dedicated for development of nonlinear photonic crystal fibers," *Opt. Mater. Express* **7**(10), 3471–3483 (2017).
20. S. Kedenburg, M. Vieweg, T. Gissibl, and H. Giessen, "Linear refractive index and absorption measurements of nonlinear optical liquids in the visible and near-infrared spectral region," *Opt. Mater. Express* **2**(11), 1588–1611 (2012).
21. K. Saitoh, M. Koshiba, T. Hasegawa, and E. Sasaoka, "Chromatic dispersion control in photonic crystal fibers: application to ultra-flattened dispersion," *Opt. Express* **11**(8), 843–852 (2003).
22. M. Chemnitz, C. Gaida, M. Gebhardt, F. Stutzki, J. Kobelke, A. Tünnermann, J. Limpert, and M. A. Schmidt, "Carbon chloride-core fibers for soliton mediated supercontinuum generation," *Opt. Express* **26**(3), 3221–3235 (2018).
23. D. Pysz, I. Kujawa, R. Stępień, M. Klimczak, A. Filipkowski, M. Franczyk, L. Kociszewski, J. Buźniak, K. Haraśny, and R. Buczynski, "Stack and draw fabrication of soft glass microstructured fiber optics," *Bull. Pol. Acad. Sci. Tech. Sci.* **62**, 667–682 (2014).
24. P. Hlubina, D. Ciprian, and R. Chlebus, "Group index dispersion of holey fibres measured by a white-light spectral interferometric technique," *Opt. Commun.* **281**(15-16), 4008–4013 (2008).
25. T. Martynkien, D. Pysz, R. Stępień, and R. Buczyński, "All-solid microstructured fiber with flat normal chromatic dispersion," *Opt. Lett.* **39**(8), 2342–2345 (2014).
26. K. Tarnowski, T. Martynkien, P. Mergo, K. Poturaj, A. Anuszkiewicz, P. Bójot, F. Billard, O. Faucher, B. Kibler, and W. Urbanczyk, "Polarized all-normal dispersion supercontinuum reaching 2.5 μm generated in a birefringent microstructured silica fiber," *Opt. Express* **25**(22), 7452–27463 (2017).
27. A.M. Heidt, "Pulse preserving flat-top supercontinuum generation in all-normal dispersion photonic crystal fibers," *J. Opt. Soc. Am. B* **27**(3), 550–559 (2010).
28. J.M. Dudley and S. Coen, "Coherence properties of supercontinuum spectra generated in photonic crystal and tapered optical fibers," *Opt. Lett.* **27**(13), 1180–1182 (2002).
29. A. M. Heidt, J. S. Feehan, J. H. V. Price, and T. Feurer, "Limits of coherent supercontinuum generation in normal dispersion fibers," *J. Opt. Soc. Am. B* **34**(4), 764–775 (2017).
30. E. Genier, P. Bowen, T. Sylvestre, J. M. Dudley, P. Moselund, and O. Bang, "Amplitude noise and coherence degradation of femtosecond supercontinuum generation in all-normal-dispersion fibers," *J. Opt. Soc. Am. B* **36**(2), A161–A167 (2019).
31. I. B. Gonzalo, R. D. Engelsholm, M. P. Sørensen, and O. Bang, "Polarization noise places severe constraints on coherence of all-normal dispersion femtosecond supercontinuum generation," *Sci. Rep.* **8**(1), 1–13 (2018).
32. V. T. Hoang, R. Kasztelanic, A. Anuszkiewicz, G. Stępniewski, A. Filipkowski, S. Ertman, D. Pysz, T. Wolinski, K. D. Xuan, M. Klimczak, and R. Buczynski, "All-normal dispersion supercontinuum generation in photonic crystal fibers with large hollow cores infiltrated with toluene," *Opt. Mater. Express* **8**(11), 3568–3582 (2018).
33. K. Nielsen, D. Noordegraaf, T. Sørensen, A. Bjarklev, and T. P. Hansen, "Selective filling of photonic crystal fibers," *J. Opt. A: Pure Appl. Opt.* **7**(8), L13–L20 (2005).

34. J. M. Dudley, G. Genty, and S. Coen, "Supercontinuum generation in photonic crystal fiber," *Rev. Mod. Phys.* **78**(4), 1135–1184 (2006).
35. I. Cristiani, R. Tedioli, L. Tartara, and V. Degiorgio, "Dispersive wave generation by solitons in microstructured optical fibers," *Opt. Express* **12**(1), 124–135 (2004).
36. A. Rampur, D.-M. Spangenberg, G. Stępniewski, D. Dobrakowski, K. Tarnowski, K. Stefańska, A. Paździor, P. Mergo, T. Martynkien, T. Feurer, M. Klimczak, and A. M. Heidt, "Temporal fine structure of all-normal dispersion fiber supercontinuum pulses caused by non-ideal pump pulse shapes," *Opt. Express* **28**(11), 16579–16593 (2020).
37. B. Sierro and A. Heidt, "Noise amplification in all-normal dispersion fiber supercontinuum generation and its impact in ultrafast photonics applications," *OSA Continuum* **3**(9), 2347–2361 (2020).
38. K. Tarnowski, T. Martynkien, P. Mergo, K. Poturaj, G. Soboń, and W. Urbańczyk, "Coherent supercontinuum generation up to 2.2 μm in an all-normal dispersion microstructured silica fiber," *Opt. Express* **24**(26), 30523–30536 (2016).
39. M. Klimczak, B. Siwicki, B. Zhou, M. Bache, D. Pysz, O. Bang, and R. Buczyński, "Coherent supercontinuum bandwidth limitations under femtosecond pumping at 2 μm in all-solid soft glass photonic crystal fibers," *Opt. Express* **24**(26), 29406–29416 (2016).
40. T. S. Saini, T. H. Tuan, T. Suzuki, and Y. Ohishi, "Coherent Mid-IR Supercontinuum Generation using Tapered Chalcogenide Step-Index Optical Fiber: Experiment and modelling," *Sci. Rep.* **10**(1), 2236 (2020).
41. A. Rampur, Y. Stepanenko, G. Stępniewski, T. Kardaś, D. Dobrakowski, D.-M. Spangenberg, T. Feurer, A. Heidt, and M. Klimczak, "Ultra low-noise coherent supercontinuum amplification and compression below 100 fs in an all-fiber polarization-maintaining thulium fiber amplifier," *Opt. Express* **27**(24), 35041–35051 (2019).
42. A. M. Heidt, J. M. Hodasi, A. Rampur, D.-M. Spangenberg, M. Ryser, M. Klimczak, and T. Feurer, "Low noise all-fiber amplification of a coherent supercontinuum at 2 μm and its limits imposed by polarization noise," *Sci. Rep.* **10**(1), 16734 (2020).